Midnight Sun to Polar Night: A Model of Seasonal Light in the Barents Sea

Stacey Connan-McGinty[1] [iD], **Neil S. Banas[2]** [iD], **Jørgen Berge[3,4,5]**, **Finlo Cottier[5,6]** [iD], **Stephen Grant[3]**, **Geir Johnsen[3,4]** [iD], **Tomasz P. Kopec[5]** [iD], **Marie Porter[6]** [iD], and **David McKee[1,5]** [iD]

[1]Department of Physics, University of Strathclyde, Glasgow, UK, [2]Department of Mathematics and Statistics, University of Strathclyde, Glasgow, UK, [3]Department of Biology, Centre for Autonomous Marine Operations and Systems, Norwegian University of Science and Technology (NTNU), Trondheim, Norway, [4]University Centre in Svalbard (UNIS), Longyearbyen, Norway, [5]Faculty of Biosciences, Fisheries and Economics, UiT The Arctic University of Norway, Tromsø, Norway, [6]Scottish Association for Marine Science, Oban, UK

Abstract Arctic marine ecosystems are strongly influenced by the extreme seasonality of light in the region. Accurate determination of light is essential for building a comprehensive understanding of the dynamics of animal and aquatic algae populations. Current approaches to underwater light field parameterisations rely upon shortwave radiation (300–3000 nm) estimates from satellites or surface radiometry measurements to populate full radiative transfer software. Due to the inaccessibility of many regions in the Arctic, measured data is not widely available. This study presents a model of spectrally resolved underwater light in ice-free conditions in the Barents Sea. Given a location and time, the model accounts for downwelling spectral irradiance in the photosynthetically active radiation (PAR, 400–700 nm) range ($E_{D\ PAR}$) at the ocean surface from solar, lunar, and galactic light sources, modulated by local cloud cover. We demonstrate the ability to extend over the full year into the period of Polar Night, validated in both broadband PAR and spectral domains. Using a bio-optical model of diffuse attenuation developed for the Barents Sea, we show accurate calculations to depth for inhomogeneous water columns over a spatial-temporal range, validated against time series irradiance data from the ArcLight observatory in Ny-Ålesund, Svalbard and in-situ irradiance sensors deployed in the Barents Sea. Finally, in comparison to state-of-the-art radiative transfer models, averaged over the water column we demonstrate a typical mean absolute error of <1 μmol m^{-2} s^{-1} in $E_{D\ PAR}$ for overcast conditions (<6 μmol m^{-2} s^{-1} for clear-sky) and reduced execution time of factor 20.

Plain Language Summary Marine organisms in the Arctic experience large variations in underwater light levels due to prolonged periods of 24-hr darkness and 24-hr light. Since light is a key driver in many ecosystem dynamics, accurate modeling of Arctic marine populations can be challenging due to difficulties in determining light levels. The harsh conditions of the region can make many areas inaccessible, and often light levels fall below the sensitivity limits of widely available commercial radiometers. Additionally, most existing light field models can only predict light when the sun is above the horizon. We present a light field model that operates uninterrupted throughout the full year, able to calculate light fields from the sun above and below the horizon as well as light from the moon. The model determines spectrally resolved underwater light levels in the wavelength range that is important for biological processes. Modeled outputs have been compared and show good agreement with above surface light measurements taken in Ny-Ålesund as well as underwater measurements recorded in the Barents Sea.

1. Introduction

The light climate in the Arctic is primarily controlled by seasonal changes in solar elevation. The region experiences extended periods of 24-hr daylight (Polar Day) and 24-hr darkness (Polar Night), resulting in extreme variations in both the magnitude and spectral composition of irradiance entering the ocean throughout the year. Whilst the sun remains below the horizon during the Polar Night, solar elevation still significantly controls spectral irradiance during much of this period through atmospheric scattering of light from the sun. However, throughout the darkest periods of the winter season, irradiance from the moon becomes the dominant source of illumination (Johnsen, Zolich, et al., 2021).

Variations in light intensity have been shown to be an important environmental cue in the behavior of marine organisms as well as a key driver in the development of phytoplankton blooms, which form the base of the Arctic food chain (Castellani et al., 2021). Recent work has shown Arctic zooplankton performing vertical migrations in response to changes in both the position and phase of the moon during Polar Night (Last et al., 2016). In the absence of moonlight, some zooplankton may also be able to both detect and utilize ambient diffuse solar light at certain wavelengths down to a depth of around 30 m during the Polar Night (Cohen et al., 2015).

Examination of Arctic microalgae has also demonstrated that phytoplankton communities in the region exhibit rapid restoration of photosynthetic capacity when re-illuminated following the period of Polar Night or after ice retreat in the spring (Kvernvik et al., 2018; Sloughter et al., 2019). Although light levels through the winter season are insufficient for primary production to occur, phytoplankton species have been shown to maintain their ability for photosynthesis throughout extreme darkness and quickly respond to artificially increased light levels (Berge et al., 2015). Likewise, living and growing brown, red, and green macroalgae have also been found during the Polar Night, such as in Kongsfjorden in January 2020 (Summers et al., 2022) with monthly average downwelling irradiance in the PAR range ($E_{D \text{ PAR}}$) of $<254 \times 10^{-6}$ μmol m^{-2} s^{-1} (average $E_{D \text{ PAR}}$ for January 2017–2020, Johnsen, Zolich, et al., 2021).

Current models of light parameterization in Arctic ecosystem studies are generally focused on above horizon solar irradiance using radiative transfer models that are dependent upon in situ radiometry measurements, the use of daily shortwave radiation estimates from satellite observations, or atmospheric models and reanalyses (Freer et al., 2021; Hill et al., 2018). In such situations these light models are missing periods of the year where there are biologically significant light levels. Assumptions in current plankton models concerning underwater light during Polar Night and transitional periods are often extremely simple, introducing uncertainty and bias that likely affects large-scale reconstructions and predictions of primary productivity (Popova et al., 2010; Sloughter et al., 2019).

Recent studies on Arctic underwater light fields have focused on the complexities of light beneath variable ice and snow (Stroeve et al., 2021; Veyssière et al., 2022), but even in open-water, ice-free conditions, considerable complexities remain, particularly the impact of low sun angles and local cloud cover on underwater irradiance. Spring-time cloud cover in the Arctic has been increasing linearly in recent decades (Schweiger, 2004), and cloud cover has been shown to significantly reduce surface irradiance levels (Pfister et al., 2003). Early summer cloud cover data have also been shown to be a predictor of sea-ice concentration in the late summer in the Arctic (Choi et al., 2014), with high cloud coverage over sea-ice covered oceans altering the albedo feedback (He et al., 2019). Inclusion of the effects of cloud cover on the magnitude of irradiance reaching the ocean surface will therefore be increasingly important as the region warms.

Continuous measurement of light fields to study these various ecosystem responses remains challenging, particularly at high latitudes. Difficulties arise from dark, cold, and icy conditions, inaccessibility of remote regions, and limitations on the sensitivity of available equipment to very low irradiance levels for much of the year. As a result, a fast, accurate and inexpensive hyperspectral light model which can capture the seasonal behavior of the Arctic light climate and fully extend throughout Polar Night would be a useful tool for many lines of both observation and model-based research.

Here we present the **H**ypersp**E**ctral **I**rradiance **M**odel for **D**iurn**A**l **L**ight **L**evels (HEIMDALL) for ice-free conditions in the Barents Sea. Our hyperspectral model can accurately determine location-specific downwelling spectral irradiance($E_D(\lambda)$) contributions from solar, lunar, and galactic components throughout the year, with modulation using local cloud cover from satellite estimates and transmission across the air-ocean boundary that considers the optical behavior of low sun angles. We incorporate a region-specific bio-optical model to accurately determine the optical properties of both homogeneous and inhomogeneous water columns, requiring only salinity and chlorophyll a concentration (indication of autotrophic phytoplankton biomass) profiles as inputs. Our model provides $E_D(\lambda)$ at 10 nm resolution in the photosynthetically active radiation (PAR, 400–700 nm) range at user specified depth and temporal resolution. Through a combination of available measured and modeled data sources, HEIMDALL can provide continuous underwater hyperspectral light field estimates from Polar Day to Polar Night. Validation is achieved using time series spectral and broadband irradiance data collected from the ArcLight observatory in Ny-Ålesund, Svalbard and in-situ broadband irradiance sensors deployed in the Barents Sea, demonstrating the ability of HEIMDALL to model the magnitude and timing of seasonal light. Note that

this model in principle has global application with the proviso of ensuring that an appropriate bio-optical model is selected for the region of interest.

2. Methods

To calculate above surface spectral irradiance, HEIMDALL requires a user supplied latitude, longitude, date, and time. With these inputs, it will determine the local solar zenith angle, lunar zenith angle and phase, and will extract satellite cloud cover data for historical light levels or request user specified cloud cover values for predictive modeling. Total irradiance is determined as the sum of the direct and diffuse solar and lunar components, reduced as a function of cloud cover as required. We have also incorporated a baseline irradiance value to represent dark-sky conditions (galactic component) in the absence of significant solar and lunar illumination, where the dominant sources of light are from scattered starlight, zodiacal light and airglow (Kolláth et al., 2020). All constituent modeled and measured light data used to build HEIMDALL are in units of $Wm^{-2} nm^{-1}$, at central wavelength values of 405–695 nm in 10 nm steps. Using the photon energy at each central wavelength, HEIMDALL outputs can be converted into quantised units of $E_{D\,PAR}$ ($\mu mol\ m^{-2}\ s^{-1}$) covering a 10 nm bandwidth or retained in units of $Wm^{-2}\ nm^{-1}$. Direct and diffuse components of light are separately transmitted across the air-ocean boundary and propagated down the water column via the Beer-Lambert Law using optical properties determined through a bio-optical model specific to the Barents Sea. We set out in detail below each step taken to determine final output irradiance values.

2.1. Above Horizon Clear Sky Solar Irradiance

The radiative transfer software Hydrolight (Mobley et al., 2001a, 2001b) uses an extension of the RADTRAN model (Gregg & Carder, 1990) to determine direct and diffuse spectral irradiance in the 300–1,000 nm range up to a maximum solar zenith value of 89°. Using Hydrolight, clear-sky spectral irradiance values were extracted for solar zenith angles 0–80° at 10° intervals in the wavelength range 405–695 nm at 10 nm intervals, with a final run at 89°. Local solar zenith is calculated to within 0.0003° accuracy using the method of Reda and Andreas (2004). Direct and diffuse spectral irradiances in units of $Wm^{-2}\ nm^{-1}$ for the given location are then determined via interpolation of the binned values extracted through Hydrolight.

2.2. Below Horizon Clear Sky Solar Irradiance

When the solar zenith angle exceeds 90° (sun below horizon), the light field is comprised only of diffuse light scattered through the Earth's atmosphere. Although the sun is no longer visible, there still exists a significant amount of light reaching the ocean surface. Note that we do not attempt to account for the Novaya Zemlya effect, a phenomenon in which atmospheric refraction results in direct rays of sunlight being visible from a solar disk that is below the horizon. Since these direct rays of sunlight are traveling almost parallel to the ocean surface, only a negligible fraction will cross the air-ocean boundary into the water column.

Downwelling spectral irradiance ($E_D(\lambda)$) was measured by Spitschan et al. (2016) at Cherry Springs State Park in the USA (41.6646°N, 77.8125°W) over a period of approximately 8 days in the summer of 2014. Figure 1a shows the recorded values of total integrated spectral irradiance as a function of solar elevation. $E_D(\lambda)$ was measured in the range 400–800 nm at 1 nm resolution with presented data reflecting only those measurements where lunar irradiance was minimal.

The data published by Spitschan et al. (2016) show an unexpected dependence on time of day when measuring irradiance as a function of solar elevation angle (Figure 1a). Irradiance values recorded for identically binned solar elevation angles varied by up to 1.5 orders of magnitude depending on the solar azimuth. This was attributed to possible differences in atmospheric conditions at dawn and dusk, however we believe the divergence is a result of incorrect solar elevation angle calculations. Figure 1b shows the Spitschan et al. data set with solar elevation angles that have been recalculated for known times and positions using Reda and Andreas (2004). Both datasets show irradiance values binned into the nearest solar elevation angle within 2° and averaged. Figure 1b strongly suggests that there was a calculation error in the original Spitschan et al. data set. After recalculation of solar angles, the apparent hysteresis has been eliminated, which is consistent with expectations.

For incorporation into HEIMDALL, the adjusted data set was further filtered for timestamps where local cloud cover was ≤10%, with wavelengths extracted to match those of the above horizon data set (Section 2.1).
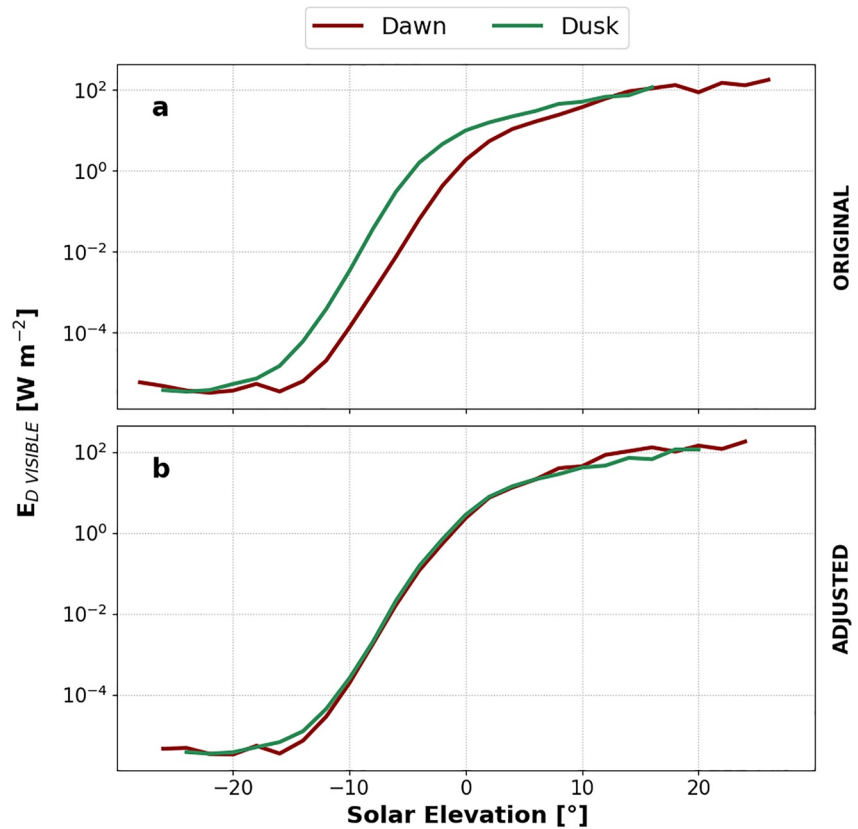
Figure 1. Total downwelling irradiance (400–800 nm) measured by Spitschan et al. (2016) as a function of (a) solar elevation as determined by Spitschan et al. (2016) (ORIGINAL), and (b) solar elevation determined using Reda and Andreas (2004) (ADJUSTED).

Appending these binned values to the existing above horizon data set and converting from solar elevation to solar zenith provides clear sky $E_D(\lambda)$ for solar light over the solar zenith range 0–110°. Irradiance is linearly interpolated for zenith angles outside of binned values.

2.3. Clear Sky Lunar Irradiance

The lunar spectral irradiance component is incorporated into HEIMDALL using existing direct and diffuse solar irradiance values. Lunar zenith, phase and distance for the given location and time are first calculated using a high precision position calculator (Rhodes, 2019). We assume a Lambertian surface reflecting equally in all directions with an apparent full-moon radiance at lunar zenith angle (θ_L) of:

$$L_{\mathrm{FM}}(\lambda, \theta_L) = \frac{\alpha(\lambda) S_D(\lambda, \theta_L)}{\pi} \tag{1}$$

where $L_{\mathrm{FM}}(\lambda, \theta_L)$ is the apparent full-moon lunar spectral radiance, $S_D(\lambda, \theta_L)$ is the equivalent solar irradiance at lunar zenith angle (θ_L), and $\alpha(\lambda)$ is spectral albedo determined from Shkuratov et al. (1999). $L_{\mathrm{FM}}(\lambda, \theta_L)$ is then multiplied by the solid angle subtended by the moon (Ω_L) at a distance calculated from the center of the Earth for the user given date, and a phase factor (F), relating lunar phase angle (ϕ) to illumination fraction (Miller & Turner, 2009). This gives lunar irradiance:

$$E_{D\,\mathrm{lunar}}(\lambda, \theta_L, \phi) = L_{\mathrm{FM}}(\lambda, \theta_L) F(\phi) \Omega_L \tag{2}$$

By using the solar irradiance at zenith θ_L rather than the solar constant, we can maintain direct and diffuse components for lunar irradiance without the need for additional inclusion of atmospheric properties.

2.4. Clear Sky Dark-Sky (Galactic) Irradiance

As shown in Figure 1, irradiance levels reach a baseline value of order 10^{-6} W m^{-2} where solar elevation is no longer a dependent variable. Light levels recorded at Zselic Starry Sky Park in Hungary (46.2366°N, 17.7653°E) measured spectral radiance contributions from starlight, sunlight scattered by interplanetary dust (zodiacal light), and the faint emission of light from atomic processes in the atmosphere (airglow), and found that the spectral composition of these components was approximately flat at a value of 2 nW m^{-2} sr^{-1} nm^{-1} (Kolláth et al., 2020). A single hemisphere of 2π steradians integrated over the 400–700 nm range gives a baseline irradiance value of approximately 3 μW m^{-2}, consistent with observations in Figure 1. In our model, a spectrally flat baseline irradiance value of 4π nW m^{-2} nm^{-1} (2 nW m^{-2} sr^{-1} nm^{-1} * 2π steradians) is applied to diffuse solar irradiance with solar zenith angle >106°. This value is determined by averaging the dawn and dusk datasets from Figure 1.

2.5. Cloud Cover Modulation

The behavior of light propagating through cloud can be optically complex, with dependencies such as cloud type and thickness. In HEIMDALL, we include a simple, spectrally flat approximation of irradiance reduction first proposed by Kasten and Czeplak (1980).

$$E_D(C_F) = E_D(0) \left(1 - 0.75 C_F^{3.4} \right) \tag{3}$$

$$E_{D\,\text{dif}}(C_F) = E_D(C_F) \left(0.3 + 0.7 C_F^2 \right) \tag{4}$$

$$E_{D\,\text{dir}}(C_F) = E_D(C_F) - E_{D\,\text{dif}}(C_F) \tag{5}$$

where $E_D(0)$, $E_D(C_F)$ are total downwelling irradiance summed from all sources for a clear sky and at cloud fraction C_F respectively. $E_{D\,\text{dif}}$, $E_{D\,\text{dir}}$ are the diffuse and direct components respectively. When the sun or moon is below the horizon and there is no clear-sky direct field, Equation 3 only is applied.

Hourly averaged estimates of fractional cloud cover at 0.25° spatial resolution are available from the Copernicus Climate Change Service (C3S) Climate Data Store (Hersbach et al., 2018). User supplied latitude and longitude is rounded to the nearest 0.25° with cloud cover data extracted for the required date and time and applied to Equations 3–5.

2.6. Air-Ocean Transmission

The above surface downwelling irradiance field is preserved as separate direct and diffuse components. The direct component is transmitted across the air-ocean boundary using Fresnel coefficients and using the local solar or lunar zenith as the angle of incidence (Mobley, 2022). Analysis of clear-sky direct and diffuse light transmission across the air-ocean boundary for increasing surface roughness was undertaken using Hydrolight. Varying windspeed from 0 ms^{-1} to 15 ms^{-1} in 2.5 ms^{-1} steps showed no significant increase in underwater light for the diffuse component (1.7% increase at 15 ms^{-1}) for all solar zenith angles. The direct component saw minimal variation for zenith angles <80° (4% increase at 15 ms^{-1}), and a significant increase of factor 3 for zenith angle 89°. At zenith 89°, the direct component of light accounts for <0.003% of the total light field. The air-ocean boundary is therefore treated as flat since surface roughness did not appear to result in a significant change in total underwater downwelling irradiance.

The diffuse light field is comprised of photons with random direction of travel, with an angle of incidence on the ocean surface ranging from 0 to 90°. Assuming an average incidence angle of 45° applied to Fresnel coefficients gives a transmittance fraction of 0.97 for diffuse light. This constant value is applied to the diffuse component of the downwelling irradiance.

2.7. Underwater Attenuation Model

Using a bio-optical model developed specifically for the Barents Sea (Kostakis et al., 2020), we parameterize the inherent optical properties of the water column by chlorophyll a concentration (Chl) and salinity (Sal) only.

Each optical component in the water column has an associated value of wavelength dependent absorption ($a(\lambda)$), scattering ($b(\lambda)$) and backscattering ($b_b(\lambda)$), the total of which are the sum of each of the constituent components.

$$a(\lambda) = a_w(\lambda) + a_{\text{CDOM}}(\lambda, \text{Sal}) + a_{\text{NAP}}(\lambda, \text{Chl}) + a_{\text{ph}}(\lambda, \text{Chl}) \tag{6}$$

$$b(\lambda) = b_w(\lambda) + b_p(\lambda, \text{Chl}) \tag{7}$$

$$b_b(\lambda) = b_{\text{bw}}(\lambda) + b_{\text{bp}}(\lambda, \text{Chl}) \tag{8}$$

where subscripts w, $CDOM$, NAP, ph, p refer to water, color dissolved organic matter, non-algal particles, phytoplankton, and particulate matter respectively. The bio-optical model uses chlorophyll a concentration (photosynthetic phytoplankton biomass) and relates all particle properties to it. It also establishes a link between salinity content and CDOM. Values for a_{CDOM}, a_{NAP}, b_p, and b_{bp} are determined from Kostakis et al. (2020), a_{ph} from Bricaud et al. (1995) and a_w, b_w, b_{bw} from Pope and Fry (1997) and Morel (1974).

Both the diffuse and direct light field are attenuated down the water column to depth z using the Beer-Lambert law.

$$E_{D\,\text{dir}}(\lambda, z) = E_{D\,\text{dir}}(\lambda, 0)\exp(-K_{\text{dir}}z) \tag{9}$$

$$E_{D\,\text{dif}}(\lambda, z) = E_{D\,\text{dif}}(\lambda, 0)\exp(-K_{\text{dif}}z) \tag{10}$$

$$K_{\text{dir}} = \frac{a(\lambda) + b_b(\lambda)}{\bar{\mu}_{\text{dir}}} \tag{11}$$

$$K_{\text{dif}} = \frac{a(\lambda) + b_b(\lambda)}{\bar{\mu}_{\text{dif}}} \tag{12}$$

where K_{dir}, K_{dif} are the diffuse attenuation coefficients of direct and diffuse light respectively and $\bar{\mu}_{\text{dir}}$, $\bar{\mu}_{\text{dif}}$ are the mean cosine values for direct and diffuse light.

Following the approach taken by Sathyendranath and Platt (1988), the value of $\bar{\mu}_{\text{dif}}$ is set to a constant value. Incident diffuse light can impact the ocean surface at an incidence angle ranging from 0 to 90°. Using Snell's law, this constrains the underwater angle of refraction to 0–48°, with mean cosine value ranging from approximately 0.67–1. We assume the midpoint value of this and set $\bar{\mu}_{\text{dif}}$ to 0.83. The value of $\bar{\mu}_{\text{dir}}$ is determined using Snell's law and the solar or lunar zenith as the angle of incidence.

To maintain the ability to process structured profiles, the water column is divided into layers of depth z' determined by the user-specified depth resolution. The depth layer is always constant at z' and the "surface" value of E_D is equal to E_D at the bottom of the previous layer.

3. Validation and Discussion

Validation of the above surface modeled light field was carried out for both $E_D(\lambda)$ and $E_{D\,\text{PAR}}$ using separate instruments located at the ArcLight light observatory (Figure 2) in Ny-Ålesund, Svalbard (78.94116°N, 11.84207°E) (Berge et al., 2021; Johnsen, Grant, et al., 2021). Underwater validation was determined using modeled results from the Hydrolight radiative transfer software for a variety of optical conditions for both broadband ($E_{D\,\text{PAR}}$) and spectral irradiance ($E_D(\lambda)$). Additionally, we have validated broadband irradiance with results from a $E_{D\,\text{PAR}}$ sensor attached to an underwater autonomous glider deployed in the Barents Sea (Figure 2) along 30°E (Kostakis et al., 2020).

3.1. Above Surface Validation

3.1.1. Spectral Irradiance

Downwelling spectral irradiance ($E_D(\lambda)$) was measured at the ArcLight observatory using an USSIMO (In-situ Marine Optics, Perth, WA, Australia) hyperspectral radiometer designed for light collection in daylight conditions. As the instrument was situated beneath a plexiglass dome, all recorded values
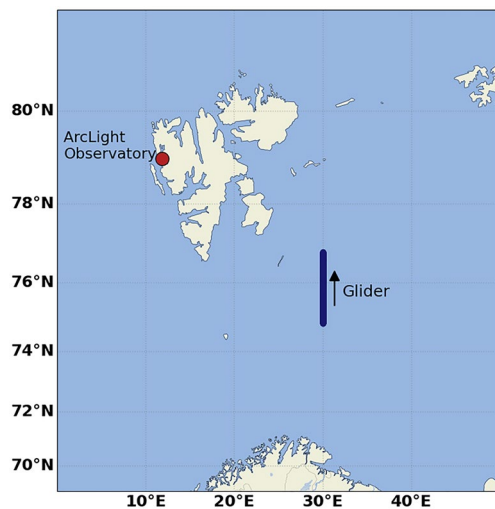
Figure 2. Location of the ArcLight Light Observatory and representative path along 30°E transect traversed by autonomous glider.
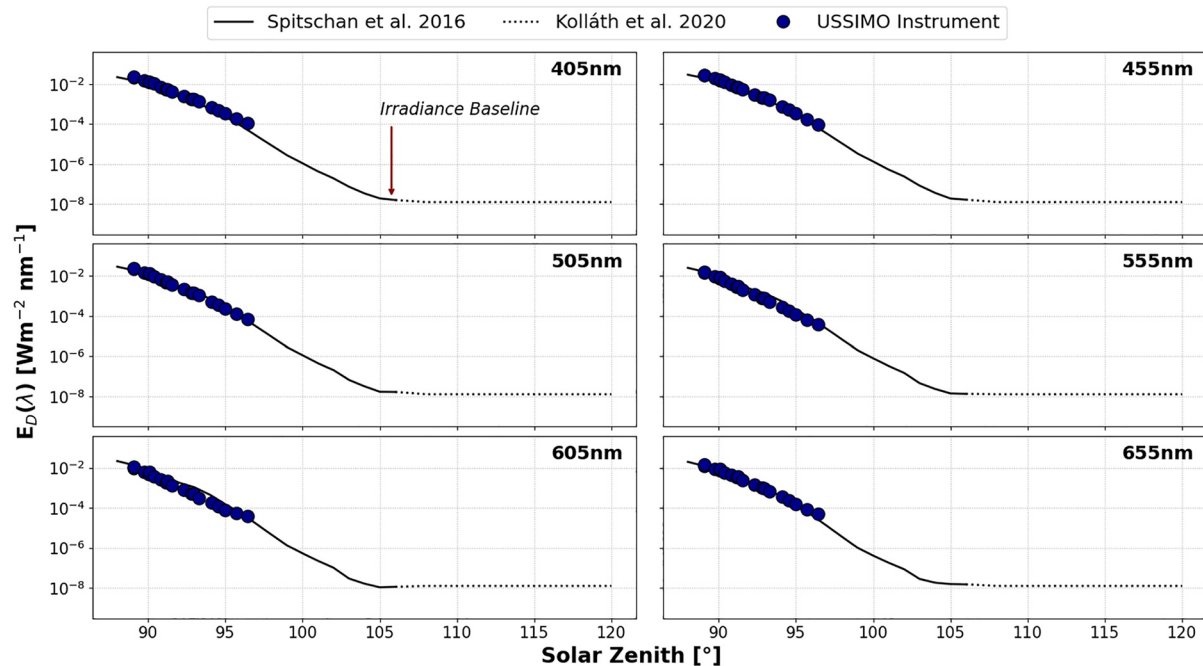
Figure 3. Spectral irradiance($E_D(\lambda)$) measured at ArcLight Observatory (symbols) and spectral irradiance values from the literature used in **H**ypersp**E**ctral **I**rradiance **M**odel for **D**iurn**A**l **L**ight **L**evels (HEIMDALL) for below horizon solar irradiance.

of $E_D(\lambda)$ were adjusted for dome transmission (Johnsen, Zolich, et al., 2021). Measurements were taken at 30-min intervals over the range 380–1,100 nm at 10 nm resolution in units of $Wm^{-2} nm^{-1}$. Solar zenith angle was calculated using our model for the observatory location and timestamp recorded by the instrument, adjusted to UTC. The detection limit of the sensor is of the order $10^{-4} Wm^{-2} nm^{-1}$ (Johnsen, Zolich, et al., 2021), which restricts measurements to a maximum zenith angle of approximately 97.5°. As a result of this limitation, measurements where zenith angle was greater than 97° have been excluded. Values recorded during February and March 2018 were extracted in the 400–700 nm range, filtered for cloud and moon free conditions, and linearly interpolated to match selected wavelengths as shown in Figure 3. Data in Figure 3 are a selection of the wavelengths implemented in HEIMDALL (405–695 nm) which were chosen to ensure consistency between modeled above and below horizon solar spectral irradiance.

Measurements at the ArcLight observatory at 79°N are in agreement with those recorded at Cherry Springs State Park at 42°N (Spitschan et al., 2016) when both are filtered for the same clear sky conditions and binned as a function of solar zenith angle. As the USSIMO instrument reaches a sensitivity limit at approximately 97° zenith, no further comparisons can be made beyond this value. Since the gradient of reduction in magnitude is consistent between both datasets, we assume the full range of values collected at 42°N are valid for use in our model. Once the solar zenith angle exceeds 106°, we apply the spectrally flat clear sky baseline irradiance value (Kolláth et al., 2020).

3.1.2. Broadband $E_{D\,PAR}$

Above surface $E_{D\,PAR}$ was recorded using a Canon D5 Mark III EOS camera (Canon Inc., Tokyo, Japan) in units of Wm^{-2} at 60-min intervals (Johnsen, Zolich, et al., 2021). To compare modeled and measured irradiance, HEIMDALL was run at the observatory location and at timestamps recorded by the instrument. Data in Figure 4 show modeled and measured $E_{D\,PAR}$ during periods of Polar Night (JAN), day/night cycling (APR) and 24-hr sunlight (JUL). Modeled output includes contributions from solar and lunar spectral irradiance, modulated by local cloud cover estimates and integrated over the PAR range.

As the fractional cloud cover value used in HEIMDALL is an hourly average for the location over the preceding 60 min, we also include a range within which real time measured irradiance values may fall. The upper and lower bounds of this range represent clear-sky and overcast conditions, respectively. There are occasional
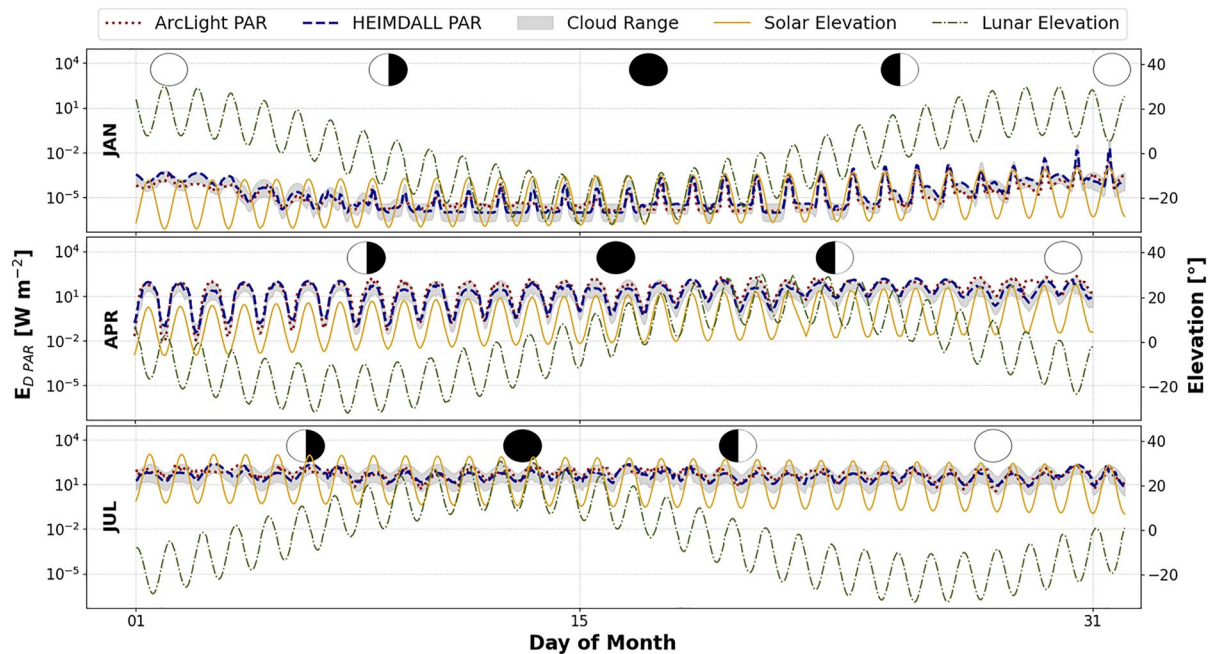
Figure 4. Modeled (dashed) and measured (dotted) $E_{D\,PAR}$ at 79°N in Spitsbergen, Svalbard in 2018. Gray shading indicates the range of variability that can be attributed to variation in cloud cover. Solar elevation (solid), lunar elevation (dash-dot) are shown along with fractional lunar illumination.

periods of mismatch where the measured value falls outside of our range of expected irradiance. We speculate that this may be a result of several factors which we cannot currently account for within HEIMDALL, for example, active precipitation, heavy fog, snow cover, aurora, local light pollution. In general, we see a good degree of match up with our model output and the measured data from the ArcLight observatory, particularly the ability to capture the behavior of the moonlight during the Polar Night both in magnitude and time. We can see this specifically in the first panel of Figure 4, where a circumpolar full moon is the dominant source of irradiance at the beginning of the month, before transitioning to a new moon on January 17th. The moon remains below the horizon from January 11th–19th inclusive and we see midday solar irradiance peaks. Although the sun is still below the horizon over this period, it has a midday zenith angle of around 100°. As the month progresses, the moon moves back above the horizon and to full moon phase on the 31st. The midday sun moves closer to the horizon, where it begins to overtake as the dominant irradiance source. We can also see a clear baseline of measured irradiance being reached of order 10^{-6} Wm^{-2}, consistent with Kolláth et al. (2020).

3.2. Below Surface Validation

3.2.1. Comparison With Hydrolight

State of the art radiative transfer models for predicting underwater light fields are available, such as the widely use proprietary software Hydrolight (Sequoia Scientific, Inc, Washington, USA). Although Hydrolight can provide very precise estimates of underwater irradiances, the process can be time expensive, is limited to above horizon solar irradiance only, and is not optimized to operate over dynamic spatial-temporal domains. To assess the capability of HEIMDALL to perform in realistic marine environments, we have compared its performance against Hydrolight for a range of optical and environmental conditions. Well-mixed, surface maximum and sub-surface maximum chlorophyll a profiles were extracted from data gathered from gliders deployed in the Barents Sea to be used as test cases, as shown in Figure 5.

For each of the three profiles, salinity was kept at a constant value of 35 PSU, a typical value for the Barents Sea region with minimal seasonal variation (Kostakis et al., 2020). Inherent optical properties were provided to both HEIMDALL and Hydrolight using the Barents Sea bio-optical model described in Section 2.7, and run for solar zenith angles of 30°, 60°, 80° and 0%, 50%, 100% cloud cover.
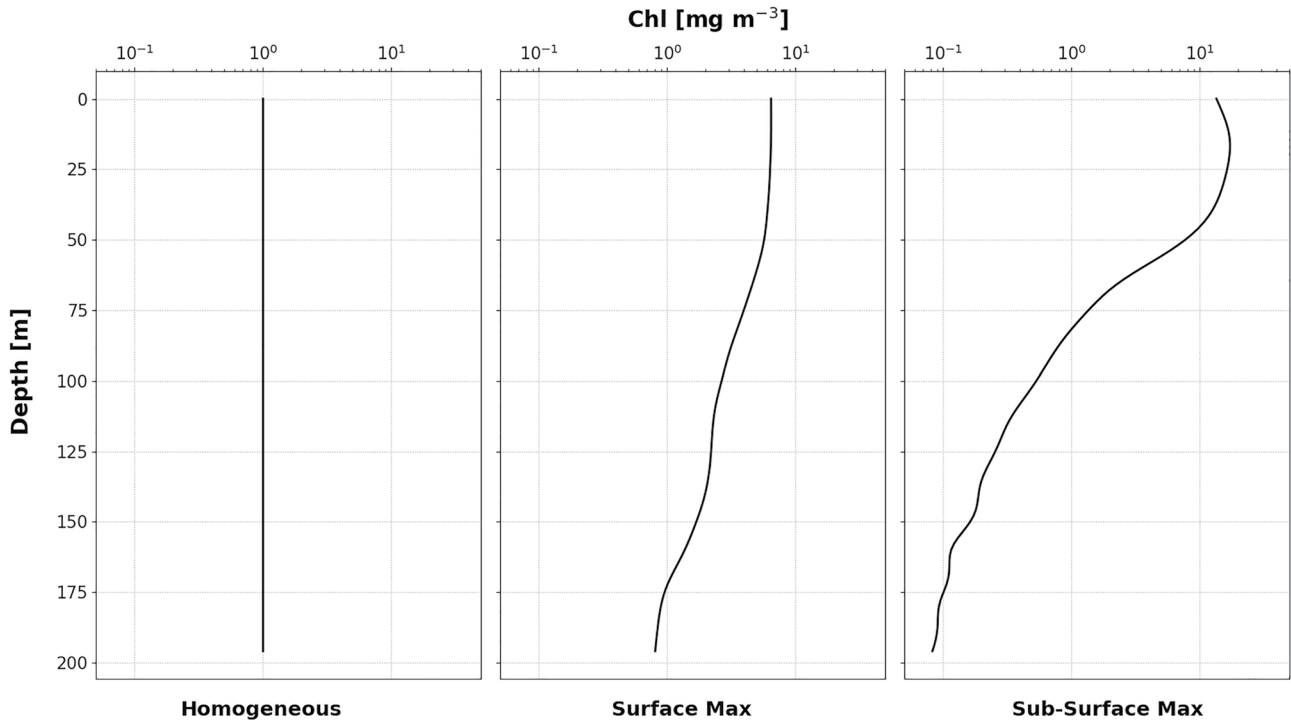
Figure 5. Input chlorophyll a profiles used to test **H**ypersp**E**ctral **I**rradiance **M**odel for **D**iurn**A**l **L**ight **L**evels (HEIMDALL) against Hydrolight.

Figure 6 shows estimates of $E_{D\,PAR}$ from HEIMDALL and Hydrolight for surface waters down to the 1% $E_{D\,PAR}$ level. The mean absolute error (MAE) for each run is shown in units of μmol m^{-2} s^{-1}. As expected, this decreases as the cloud cover increases for each simulation due to the smaller surface light levels. For a wide range of conditions, we see minimal variability in the performance of HEIMDALL compared with Hydrolight. MAE was
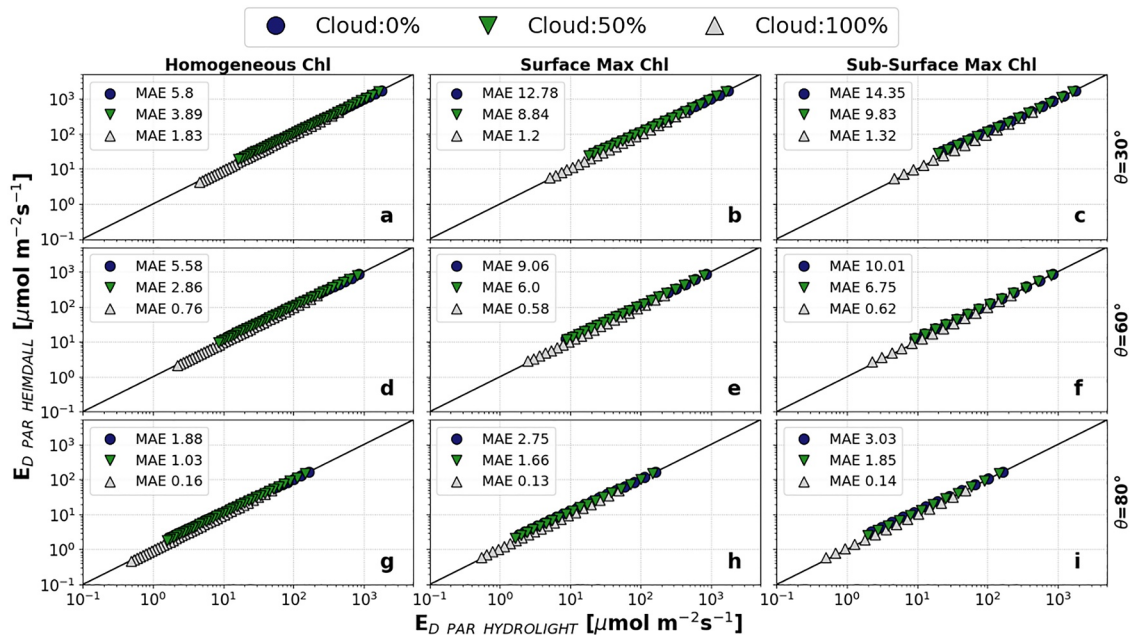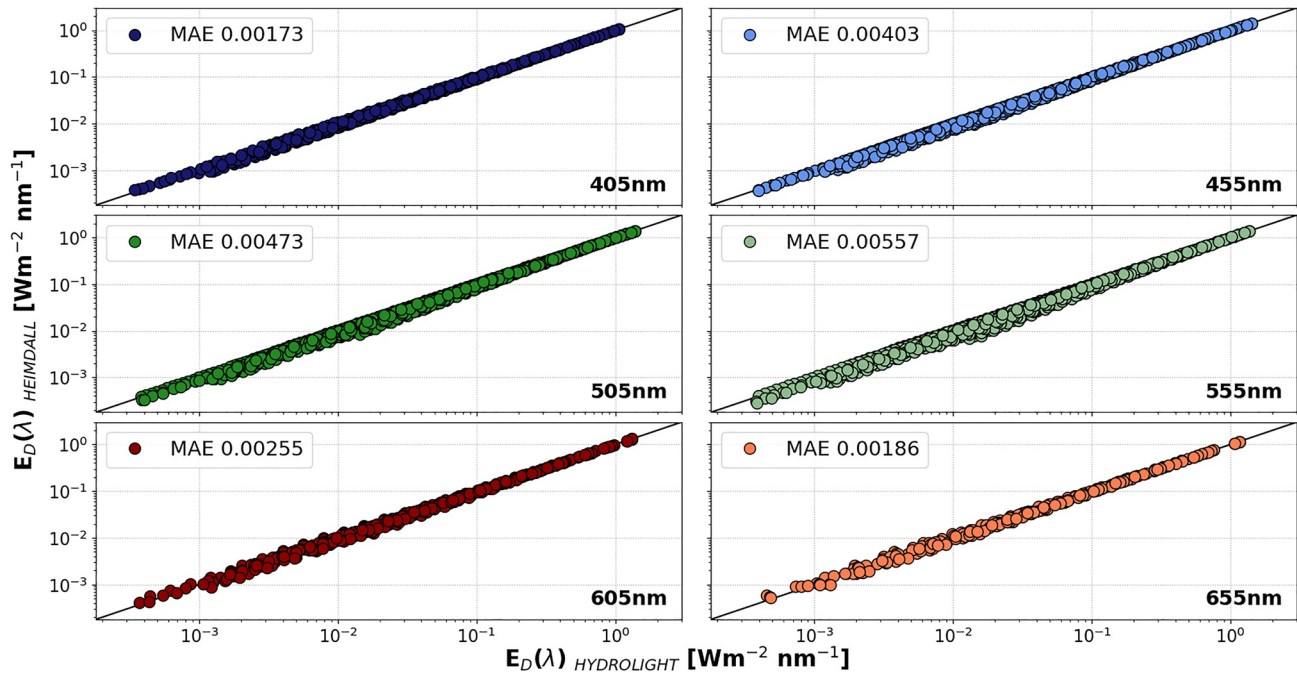

Figure 6. $E_{D\,PAR}$ from Hydrolight and **H**ypersp**E**ctral **I**rradiance **M**odel for **D**iurn**A**l **L**ight **L**evels (HEIMDALL) for various optical and environmental conditions. Values shown cover depth from surface to 1% light level. Mean absolute error (MAE) shown for each run, in units of μmol m^{-2} s^{-1}.

Figure 7. Aggregated $E_D(\lambda)$ from Hydrolight and **H**yersp**E**ctral **I**rradiance **M**odel for **D**iurn**A**l **L**ight **L**evels (HEIMDALL) for selected wavelengths. Values shown cover depth from surface to 1% light level. Mean absolute error (MAE) shown for each run, in units of Wm^{-2} nm^{-1}.

chosen as a preferred performance indicator due to the large range of magnitudes. Mean absolute percentage error (MAPE) was noted for each run but was heavily skewed by smaller values at depth. The maximum MAPE value was 23.3% for a sub-surface (chlorophyll a) maximum at 80° zenith and 0% cloud cover (Figure 6i). The minimum MAPE value was 2.2% for a homogenous water column at 80° zenith and 100% cloud cover (Figure 6g).

Figure 7 shows aggregate spectral irradiances from HEIMDALL compared to Hydrolight values for selected wavelengths and for all optical and environmental conditions tested. $E_D(\lambda)$ MAE is shown for each wavelength in units of Wm^{-2} nm^{-1}. MAE is lower for red wavelengths as rapid absorption in surface layers leads to generally small values. For each of the wavelengths shown, the MAE is relatively small compared to overall irradiance levels and we have found that these results are typical for all wavelengths across the PAR range.

Extending comparisons of both $E_{D\ PAR}$ and spectral irradiance calculations to a full depth of 200 m (not shown), we see similar performance for HEIMDALL compared with Hydrolight. The MAPE continues to be heavily weighted by errors in very small light levels at depth, with the largest full depth MAPE being 261% for a sub-surface maximum chlorophyll a profile at 30° zenith and 0% cloud cover, however this represents a MAE of 2.69 μmol m^{-2} s^{-1} where $E_{D\ PAR}$ spans 8 orders of magnitude.

Hydrolight is designed to provide a full representation of the light field while HEIMDALL is restricted to downwards irradiance only. As a result, HEIMDALL is able to produce E_D profiles faster than Hydrolight. A typical 200 m depth profile is produced by HEIMDALL in approximately 15 s and is independent of column structure, compared to >23 s for Hydrolight for a homogeneous water column and >300 s for a structured column. Simulations were run using an Intel® Core™ i7-9750H CPU at 2.60 GHz.

3.2.2. Comparison With Glider Data

Model output was also compared against $E_{D\ PAR}$ data collected from underwater gliders in the Barents Sea (Porter et al., 2020a). Autonomous G2 Slocum gliders (Teledyne, California, USA) were deployed along 30°E from January to June 2018 equipped with an $E_{D\ PAR}$ sensor (Biospherical Instruments Inc, San Diego, USA),
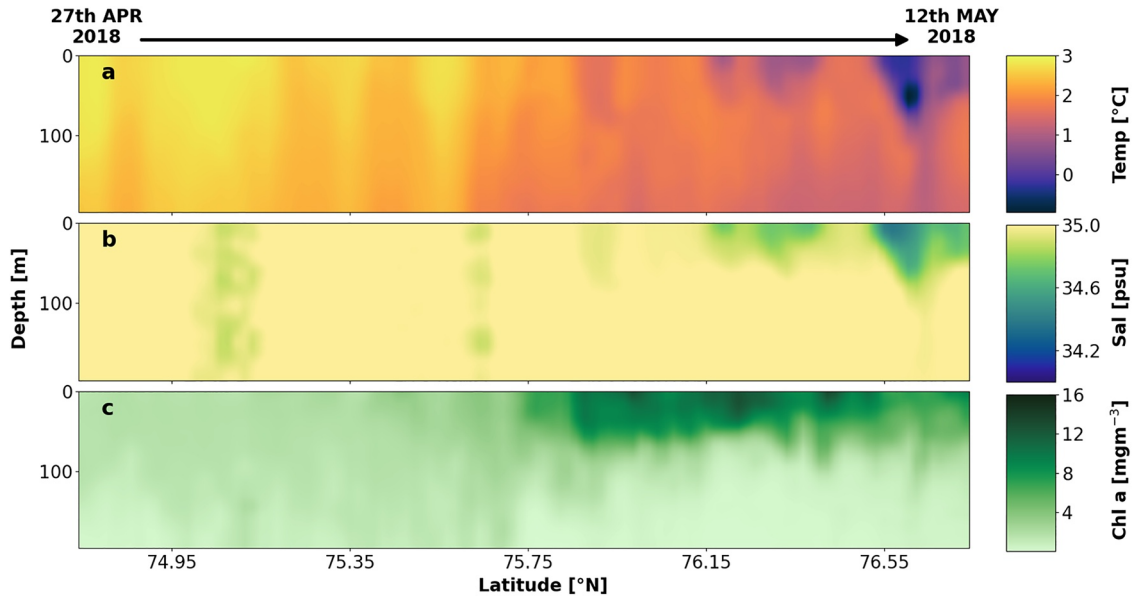
Figure 8. Profiles of (a) temperature, (b) salinity, and (c) chlorophyll a concentration collected via autonomous glider in the Barents Sea during Spring 2018. Note the occurrence of the spring bloom north of 75.75°N.

CTD sensor for temperature, salinity, and depth (Sea-bird Scientific, Washington, USA) and ECO-triplet sensor to estimate concentration of chlorophyll a, CDOM and total backscattering at 700 nm (WET Labs Inc, Oregon, USA). Data collected from this campaign and used as inputs for testing our model were salinity, chlorophyll a concentration and backscatter at 700 nm. Chlorophyll a concentration was determined by in situ chlorophyll a fluorescence (Chl_{fl}) when $Chl_{fl} \leq 2$ mgm^{-3} and via backscattering when $Chl_{fl} > 2$ mgm^{-3} (Kostakis et al., 2020). Inherent optical properties were then calculated using the bio-optical model for the region described in Section 2.7.

The period of 27 April 2018–12 May 2018 covers 406 individual depth profiles collected in a sawtooth pattern from 74.75°N to 76.73°N, where one depth profile is defined as surface to depth and back to surface. This time period was chosen for validation as it contained the largest data set collected from a single transect during the campaign. Figure 8 details the measured profiles across the collection period after undergoing gridded interpolation into equidistant latitudes and depths.

Recorded timestamps from individual raw profiles were imported into HEIMDALL to calculate local solar and lunar positions and cloud cover, with the pressure measurements in decibars from the CTD used as output depths in meters. A comparison of modeled and measured $E_{D\ PAR}$ is shown in Figure 9. A sample of 4 the 406 measured profiles have been shown for comparison, chosen via pseudo-random number generator.

Glider data were not collected at regularly spaced intervals during profiles and so a direct comparison of modeled and measured light cannot be made in terms of quantifying error. However, we do show that our estimates of light levels for similarly spaced depths are consistent and there is good agreement in the gradient of the light attenuation throughout the column for each profile. Measured $E_{D\ PAR}$ appears to hit a sensitivity baseline value around 10^{-2} μmol m^{-2} s^{-1}, below which it is no longer reliable.

For a large-scale overview of modeled and measured $E_{D\ PAR}$, data from HEIMDALL and the glider were gridded using a Barnes Objective Analysis approach for irregularly spaced data. Each of the modeled and measured datasets were interpolated using the same method and parameters. Figure 10 shows $E_{D\ PAR}$ that has been mapped for equidistant latitudes and depths.

The modeled data demonstrate good agreement in both time and magnitude of measured underwater $E_{D\ PAR}$. Figure 10 also highlights the ability of HEIMDALL to significantly extend data availability several orders of magnitude beyond the sensitivity limit of the on-board $E_{D\ PAR}$ sensor.
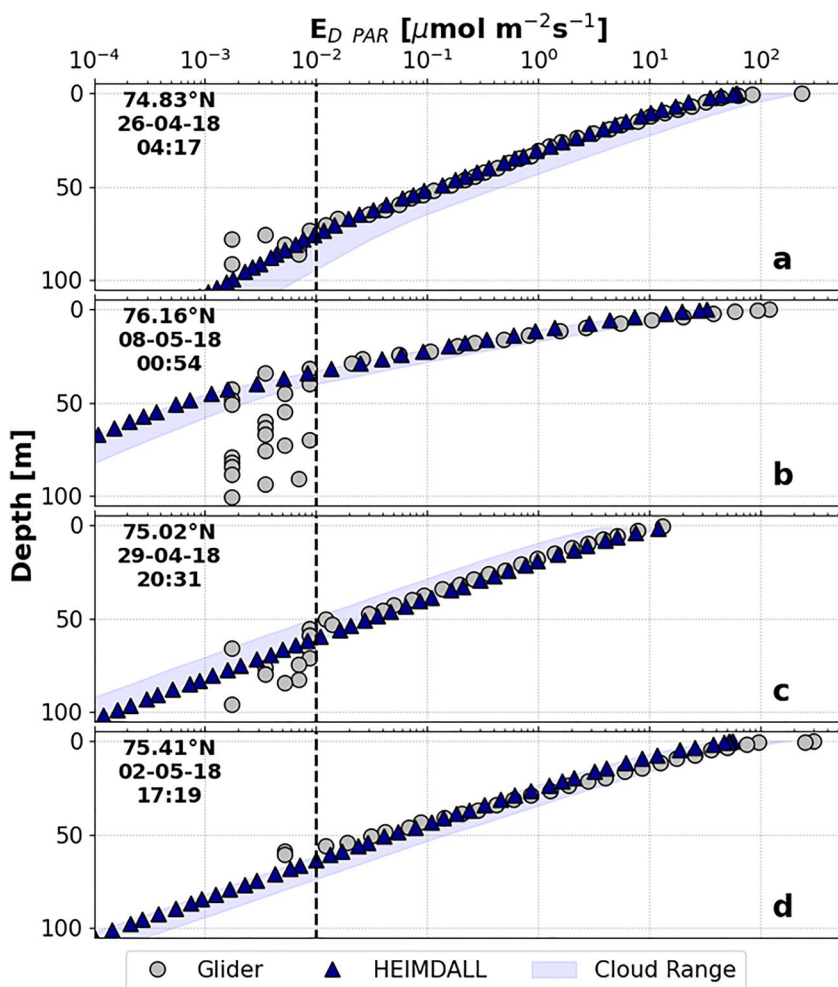
Figure 9. Modeled and measured $E_{D\ PAR}$ from the Barents Sea during 2018. Shaded blue area is possible range of $E_{D\ PAR}$ depending on local cloud cover. Dashed vertical line represents lower limit of reliability of glider measured $E_{D\ PAR}$.
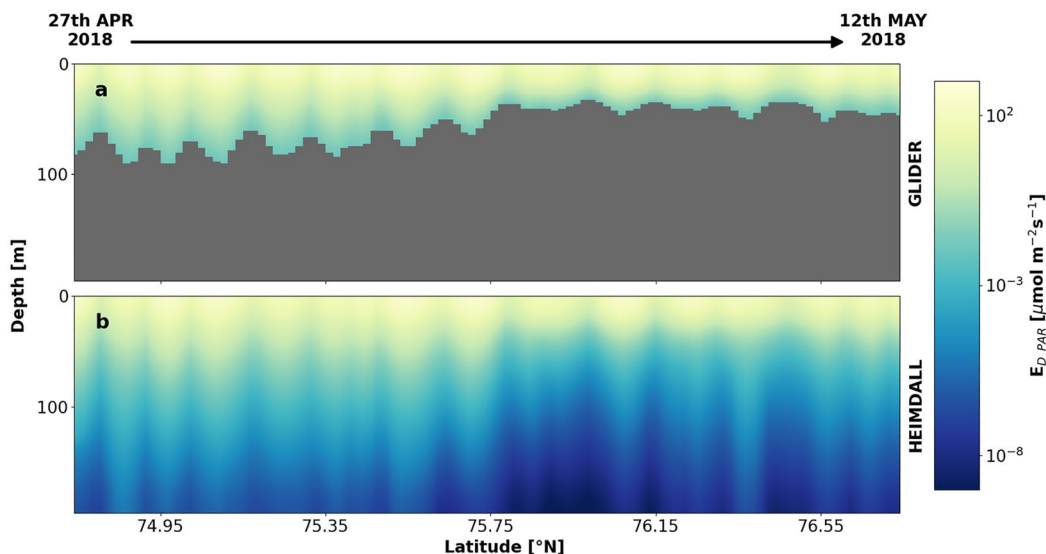
Figure 10. (a) Measured (GLIDER) and (b) modeled (**H**ypersp**E**ctral **I**rradiance **M**odel for **D**iurn**A**l **L**ight **L**evels [HEIMDALL]) $E_{D\ PAR}$ from the Barents Sea during 2018 after gridding process. Data shown is for equidistant latitudes and depths. Measured data below the light sensor sensitivity limit has been masked.
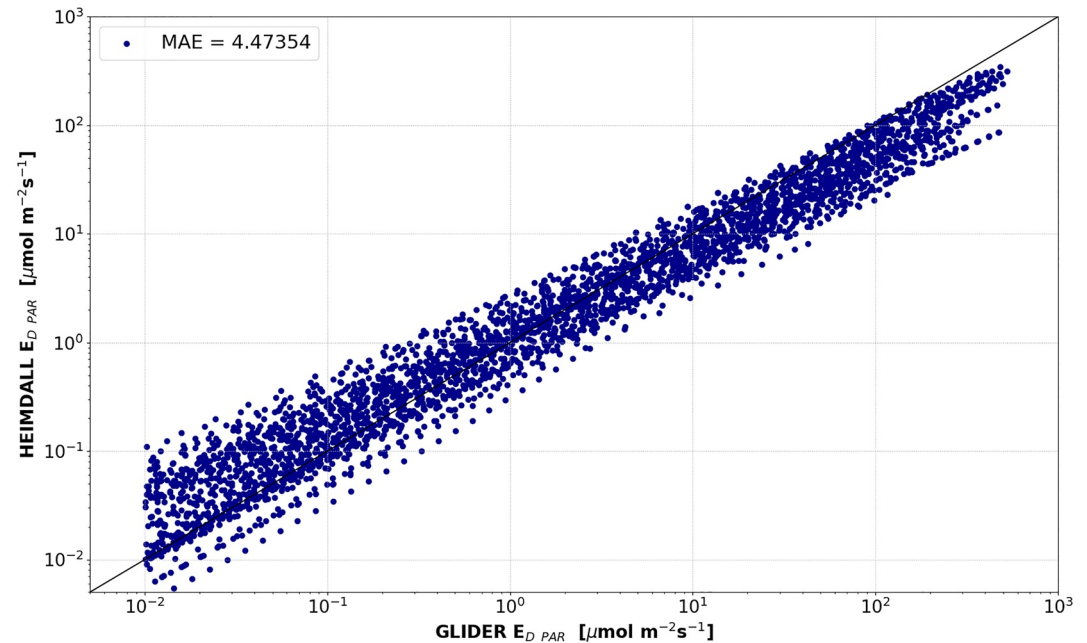
Figure 11. Direct comparison of modeled (**H**yspersp**E**ctral **I**rradiance **M**odel for **D**iurn**A**l **L**ight **L**evels [HEIMDALL]) and measured (GLIDER) $E_{D\,PAR}$ profiles from the Barents Sea after the gridding process of each data set. Mean absolute error (MAE) is shown in units of µmol m^{-2} s^{-1}.

Figure 11 demonstrates a direct comparison between the measured and modeled $E_{D\,PAR}$ profiles after gridding with associated MAE. Note that the gridded data profiles presented in Figure 11 are not directly comparable to the raw data profiles presented in Figure 9. The data shown in Figure 9 are a comparison of direct photosynthetically active radiation (PAR) measured in situ against PAR modeled using measured bio-optical data. Data presented in Figure 11 are a comparison of two interpolated datasets. Disagreement between these data at larger magnitudes is likely due to cloud cover variation, highlighted in Figure 9. At lower magnitudes, it is likely that erroneous measurements recorded by the PAR sensor due to limitations in equipment sensitivity have introduced biases during the interpolation process. Occasionally the sensor would reach a measurement plateau (as seen in Figure 9d), however more frequently it would record negative PAR values, introducing an inflated reduction in nearby interpolated data.

3.3. Applications

Due to unforeseen technical issues, gliders deployed during the Arctic PRIZE Barents Sea campaign were not equipped with an $E_{D\,PAR}$ sensor from January to April but did carry CTDs and ECO-triplet sensors (Porter et al., 2020b). HEIMDALL is therefore able to model the predicted light field for this time period when no in situ $E_{D\,PAR}$ data are available. Figure 12 shows measured temperature and salinity, and HEIMDALL estimates of $E_{D\,PAR}$ during a single north-to-south transect in February 2018. During this period the chlorophyll a concentration was beneath the limit of detection of the ECO-triplet sensor and so has been assigned a value of 0 throughout. A total of 64 individual profiles were collected and gridded using the same process as in Section 3.2.2.

Figure 12c shows HEIMDALL predicted levels of $E_{D\,PAR}$ for the week 7–13 February 2018 along with solar elevation angles for the surface time and location of each profile. During this period, the region is transitioning out of Polar Night as the sun moves closer to the horizon. For much of this period $E_{D\,PAR}$ levels are below the 10^{-2} µmol m^{-2} s^{-1} threshold identified previously and in situ $E_{D\,PAR}$ sensors would not have provided reliable data even if they had been deployed. Similarly, during this period the solar elevation is often below the horizon and Hydrolight would not be able to provide modeled estimates of underwater $E_{D\,PAR}$. Under these circumstances HEIMDALL provides a unique and viable route to establishing underwater light climate.

$E_{D\,PAR}$ is widely used as an indicator of light levels at depth in many studies of animal behavior as well as phytoplankton dynamics (Banas et al., 2016; Randelhoff et al., 2020; Wallace et al., 2010), despite the fact that marine organisms are sensitive to more limited parts of the visible spectrum (Cohen & Forward, 2002). An additional
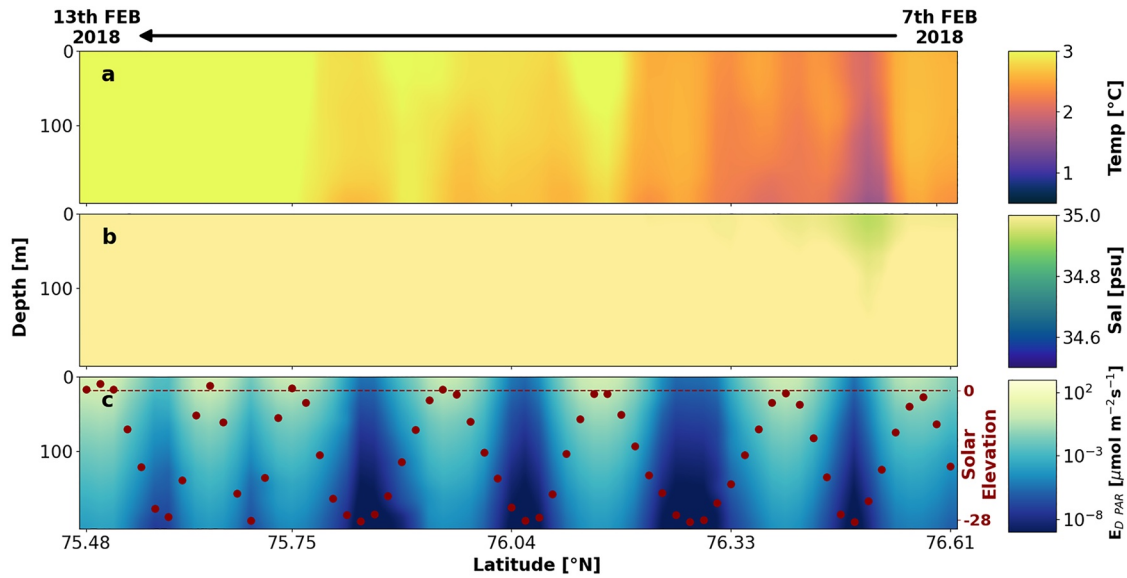
Figure 12. Measured temperature and salinity (a, b) modeled $E_{D\ PAR}$ (c) from the Barents Sea during 2018 after gridding process. Data shown is for equidistant latitudes and depths. Calculated solar elevation is displayed on panel (c), showing the solar elevation (symbols) transitioning above horizon (dashed line).

benefit of HEIMDALL is the ability to deconstruct light fields into spectral bands. Underwater spectral irradiance measurements are generally less sensitive than $E_{D\ PAR}$ measurements and even when available are therefore likely to be even more restricted in terms of depth and time periods where there are adequate signal levels. By providing hyperspectral underwater light fields, HEIMDALL provides a route to establish a better understanding of how light fields might be perceived by different marine animals.

Figure 13 illustrates how different parts of the spectrum attenuate at different rates. Red wavelengths (Figure 13a) are rapidly absorbed by water and penetrate least. In these waters green and blue wavelengths (Figures 13b and 13c) both penetrate to greater depths, with green light generally penetrating more than blue due to the presence of CDOM attenuating the shorter wavelengths. There is therefore considerable variation in the spectral composition of light with depth that is not reflected in the $E_{D\ PAR}$ data (Figure 13d). It is worth noting that the chlorophyll a transect shown in Figure 8c indicates that the glider first encountered the spring bloom at and north
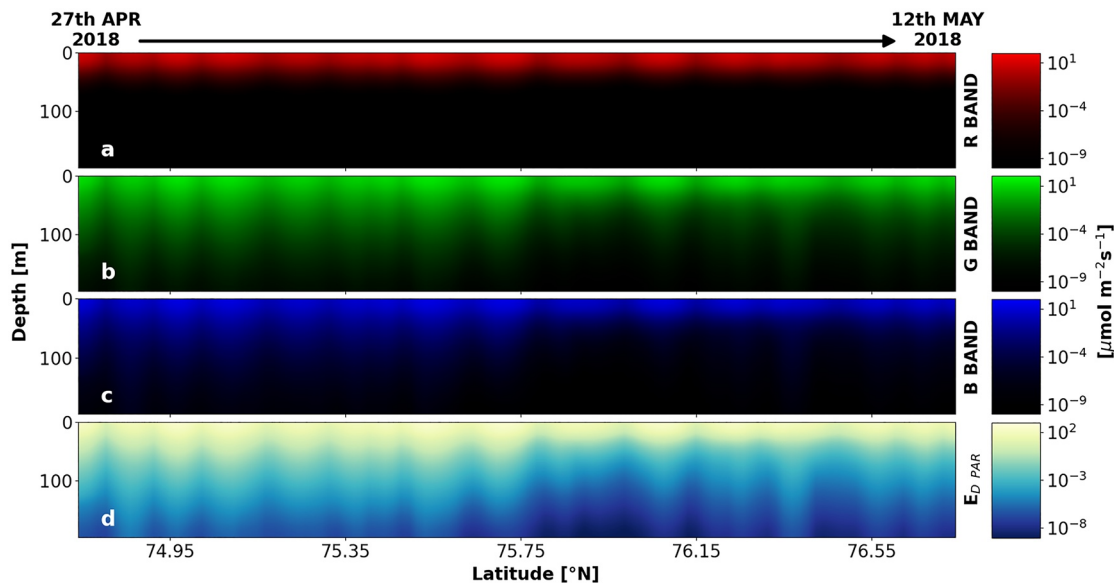
Figure 13. Modeled RGB wavebands (a–c) and $E_{D\ PAR}$ (d) for the same Barents Sea glider transect as shown previously in Figure 10.

of 75.75 N. There is a marked decline in the availability of blue light north of this transition point as a result of enhanced absorption of blue light by algal pigments.

4. Discussion and Conclusions

Light measurement in Arctic waters continues to be a challenge due to extended periods of low light to "dark" light conditions, requiring sensitive equipment as well as difficulty in accessing many areas. We have presented a hyperspectral model of underwater light that is able to provide fast and accurate light field estimates for the Barents Sea, capturing seasonal solar and lunar irradiance with modulation by local cloud conditions. HEIMDALL extends the range of light conditions that can be modeled beyond the capacity of Hydrolight, enabling estimation of underwater light levels during Polar Night when the sun is below the horizon. This is achieved whilst maintaining broad agreement with the more sophisticated Hydrolight radiative transfer model and providing a computationally efficient solution.

The ability to predict spectrally resolved light fields to depth and inclusion of a complete solar/lunar/galactic surface light model means HEIMDALL will be a useful tool in the study of estimating light induced primary production as a function of time and space, providing depth resolved primary production estimates with the provision of either a spectral or broadband primary production model. Furthermore, HEIMDALL can be directly integrated into models of phytoplankton bloom dynamics and animal behavior studies across the full annual cycle, filling gaps in existing datasets, particularly at high latitudes. Fully customizable depth and time resolution steps mean it should be possible to provide useful information for static positions (e.g., observatories on land, fixed moorings at sea) or for mobile operations (e.g., autonomous vehicles or tagged animals). The key limitation is a need to populate and define a suitable bio-optical model for the region of interest. Here we have demonstrated that the bio-optical model for the Barents Sea proposed by Kostakis et al. (2020) performs well in this region and can be adequately populated using information provided by commonly deployed in situ sensors (CTD and ECO-triplet). HEIMDALL could be easily adapted for operation in other regions through adaptation of the bio-optical model for the region of interest and ensuring that there was an adequate supply of in situ information to populate it. The above surface light field inputs, including cloud cover, are already global.

One remaining challenge of modeling light in the Arctic is the presence of ice, melt ponds and snow cover on the surface of the ocean. These inhomogeneous structures are widely recognised to pose a significant challenge in modeling the optical processes involved (Stroeve et al., 2021), but it is clear that since light is heavily attenuated after propagation through snow and ice there is a real need to provide at least a reasonable first approximation. Development of a suitable snow and ice transmission module is an ambition for a future version of HEIMDALL.

Data Availability Statement

Data supplement is available from https://doi.org/10.5281/zenodo.7041939 and contains modeled data and code to reproduce all figures from this paper. Figures were created using Python version 3.7 available under the PSF License Agreement for Python at https://www.python.org. The full HEIMDALL open water hyperspectral light model is available under the Creative Commons Attribution 4.0 License at https://doi.org/10.5281/zenodo.7048953. Cloud cover data is provided by the European Centre for Medium-Range Weather Forecasts (ECMWF) ERA5 Reanalysis. ERA5 hourly data on single levels from 1959 to present can be accessed at cds.climate.copernicus.eu.

References

Banas, N. S., Zhang, J., Campbell, R. G., Sambrotto, R. N., Lomas, M. W., Sherr, E., et al. (2016). Spring plankton dynamics in the Eastern Bering Sea, 1971–2050: Mechanisms of interannual variability diagnosed with a numerical model. *Journal of Geophysical Research: Oceans*, *121*(2), 1476–1501. https://doi.org/10.1002/2015JC011449

Berge, J., Daase, M., Renaud, P., Ambrose, W., Darnis, G., Last, K., et al. (2015). Unexpected levels of biological activity during the polar night offer new perspectives on a warming Arctic. *Current Biology*, *25*(19), 2555–2561. https://doi.org/10.1016/j.cub.2015.08.024

Berge, J., Grant, S., Bjørgum, R., Cohen, J. H., McKee, D., Johnsen, G., et al. (2021). USSIMO spectroradiometer raw data time series (2018) measured under the dome of a light observatory in the Arctic (Ny-Ålesund, Svalbard, Norway). *Norstore*. https://doi.org/10.11582/2021.00044

Bricaud, A., Babin, M., Morel, A., & Claustre, H. (1995). Variability in the chlorophyll-specific absorption coefficients of natural phytoplankton: Analysis and parameterization. *Journal of Geophysical Research*, *100*(C7), 13321. https://doi.org/10.1029/95jc00463

Castellani, G., Veyssière, G., Karcher, M., Stroeve, J., Banas, S., Bouman, A., et al. (2021). Shine a light: Under-ice light and its ecological implications in a changing Arctic Ocean. *Ambio*, *51*(2), 307–317. https://doi.org/10.1007/s13280-021-01662-3

Choi, Y.-S., Kim, B.-M., Hur, S.-K., Kim, S.-J., Kim, J.-H., & Ho, C.-H. (2014). Connecting early summer cloud-controlled sunlight and late summer sea ice in the Arctic. *Journal of Geophysical Research: Atmospheres*, *119*(19), 11087–11099. https://doi.org/10.1002/2014JD022013

Cohen, J., Berge, J., Moline, M., Sørensen, A., Last, K., Falk-Petersen, S., et al. (2015). Is ambient light during the high Arctic polar night sufficient to act as a visual cue for zooplankton? *PLoS One*, *10*(6), e0126247. https://doi.org/10.1371/journal.pone.0126247

Cohen, J., & Forward, R. (2002). Spectral sensitivity of vertically migrating marine copepods. *The Biological Bulletin*, *203*(3), 307–314. https://doi.org/10.2307/1543573

Freer, J., Daase, M., & Tarling, G. (2021). Modelling the biogeographic boundary shift of Calanus finmarchicus reveals drivers of Arctic Atlantification by subarctic zooplankton. *Global Change Biology*, *28*(2), 429–440. https://doi.org/10.1111/gcb.15937

Gregg, W., & Carder, K. (1990). A simple spectral solar irradiance model for cloudless maritime atmospheres. *Limnology & Oceanography*, *35*(8), 1657–1675. https://doi.org/10.4319/lo.1990.35.8.1657

He, M., Hu, Y., Chen, N., Wang, D., Huang, J., & Stamnes, K. (2019). High cloud coverage over melted areas dominates the impact of clouds on the albedo feedback in the Arctic. *Scientific Reports*, *9*(1), 9529. https://doi.org/10.1038/s41598-019-44155-w

Hersbach, H., Bell, B., Berrisford, P., Biavati, G., Horányi, A., Muñoz Sabater, J., et al. (2018). ERA5 hourly data on single levels from 1979 to present. *Copernicus Climate Change Service (C3S) Climate Data Store (CDS)*. https://doi.org/10.24381/cds.adbb2d47

Hill, V., Light, B., Steele, M., & Zimmerman, R. (2018). Light availability and phytoplankton growth beneath Arctic Sea Ice: Integrating observations and modeling. *Journal of Geophysical Research: Oceans*, *123*(5), 3651–3667. https://doi.org/10.1029/2017jc013617

Johnsen, G., Grant, S., Bjørgum, R., Cohen, J. H., McKee, D., Kopec, T. P., et al. (2021). Time series (2018) of irradiance in the PAR (photosynthetically active radiation) region measured under the dome of a light observatory in the Arctic (Ny-Ålesund, Svalbard, Norway) derived from SLR camera. *Norstore*. https://doi.org/10.11582/2021.00048

Johnsen, G., Zolich, A., Grant, S., Bjørgum, R., Cohen, J., McKee, D., et al. (2021). All-sky camera system providing high temporal resolution annual time series of irradiance in the Arctic. *Applied Optics*, *60*(22), 6456. https://doi.org/10.1364/ao.424871

Kasten, F., & Czeplak, G. (1980). Solar and terrestrial radiation dependent on the amount and type of cloud. *Solar Energy*, *24*(2), 177–189. https://doi.org/10.1016/0038-092x(80)90391-6

Kolláth, Z., Cool, A., Jechow, A., Kolláth, K., Száz, D., & Tong, K. (2020). Introducing the dark sky unit for multi-spectral measurement of the night sky quality with commercial digital cameras. *Journal of Quantitative Spectroscopy and Radiative Transfer*, *253*, 107162. https://doi.org/10.1016/j.jqsrt.2020.107162

Kostakis, I., Röttgers, R., Orkney, A., Bouman, H., Porter, M., Cottier, F., et al. (2020). Development of a bio-optical model for the Barents Sea to quantitatively link glider and satellite observations. *Philosophical Transactions of the Royal Society A: Mathematical, Physical & Engineering Sciences*, *378*(2181), 20190367. https://doi.org/10.1098/rsta.2019.0367

Kvernvik, A. C., Hoppe, C. J. M., Lawrenz, E., Prášil, O., Greenacre, M., Wiktor, J. M., & Leu, E. (2018). Fast reactivation of photosynthesis in arctic phytoplankton during the polar night1. *Journal of Phycology*, *54*(4), 461–470. https://doi.org/10.1111/jpy.12750

Last, K. S., Hobbs, L., Berge, J., Brierley, A. S., & Cottier, F. (2016). Moonlight drives ocean-scale mass vertical migration of zooplankton during the Arctic winter. *Current Biology*, *26*(2), 244–251. https://doi.org/10.1016/j.cub.2015.11.038

Miller, S. D., & Turner, R. E. (2009). A dynamic lunar spectral irradiance data set for NPOESS/VIIRS day/night band night time environmental applications. *IEEE Transactions on Geoscience and Remote Sensing*, *47*(7), 2316–2329. https://doi.org/10.1109/TGRS.2009.2012696

Mobley, C. D. (2001a). Hydrolight 4. 2 technical documentation (p. 79). Retrieved from www.sequoiasci.com

Mobley, C. D. (2001b). Hydrolight 4. 2 users' guide (p. 88). Retrieved from www.sequoiasci.com

Mobley, C. D. (2022). *The oceanic optics book. Dartmouth, NS, Canada* (p. 924). International Ocean Colour Coordinating Group. https://doi.org/10.25607/OBP-1710

Morel, A. (1974). Optical properties of pure water and pure seawater. In N. G. Jerlov & E. S. Nielsen (Eds.), *Optical aspects of oceanography*. Academic Press.

Pfister, G., McKenzie, R., Liley, J., Thomas, A., Forgan, B., & Long, C. (2003). Cloud coverage based on all-sky imaging and its impact on surface solar irradiance. *Journal of Applied Meteorology*, *42*(10), 1421–1434. https://doi.org/10.1175/1520-0450

Pope, R., & Fry, E. (1997). Absorption spectrum (380–700 nm) of pure water II Integrating cavity measurements. *Applied Optics*, *36*(33), 8710. https://doi.org/10.1364/ao.36.008710

Popova, E. E., Yool, A., Coward, A. C., Aksenov, Y. K., Alderson, S. G., De Cuevas, B. A., & Anderson, T. R. (2010). Control of primary production in the Arctic by nutrients and light: Insights from a high resolution ocean general circulation model. *Biogeosciences*, *7*(11), 3569–3591. https://doi.org/10.5194/bg-7-3569-2010

Porter, M., Cottier, F. R., Dumont, E., & Venables, E. (2020a). *Arctic PRIZE mission three near-real time glider dataset in the Barents Sea Spring 2018*. British Oceanographic Data Centre, National Oceanography Centre. https://doi.org/10.5285/9e4a232d-b59e-7e87-e053-6c86abc0f29f

Porter, M., Cottier, F. R., Dumont, E., & Venables, E. (2020b). *Arctic PRIZE mission two near-real time glider dataset in the Barents Sea Winter 2018*. British Oceanographic Data Centre, National Oceanography Centre. https://doi.org/10.5285/9e4a232d-b59d-7e87-e053-6c86abc0f29f

Randelhoff, A., Lacour, L., Marec, C., Leymarie, E., Lagunas, J., Xing, X., et al. (2020). Arctic mid-winter phytoplankton growth revealed by autonomous profilers. *Science Advances*, *6*(39). https://doi.org/10.1126/sciadv.abc2678

Reda, I., & Andreas, A. (2004). Solar position algorithm for solar radiation applications. *Solar Energy*, *76*(5), 577–589. https://doi.org/10.1016/j.solener.2003.12.003

Rhodes, B. (2019). *Skyfield: High precision research-grade positions for planets and Earth satellites generator*. Astrophysics Source Code Library.

Sathyendranath, S., & Platt, T. (1988). The spectral irradiance field at the surface and in the interior of the ocean: A model for applications in oceanography and remote sensing. *Journal of Geophysical Research*, *93*(C8), 9270. https://doi.org/10.1029/jc093ic08p09270

Schweiger, A. J. (2004). Changes in seasonal cloud cover over the Arctic seas from satellite and surface observations. *Geophysical Research Letters*, *31*(12), 1–5. https://doi.org/10.1029/2004GL020067

Shkuratov, Y., Starukhina, L., Hoffmann, H., & Arnold, G. (1999). A model of spectral albedo of particulate surfaces: Implications for optical properties of the moon. *Icarus*, *137*(2), 235–246. https://doi.org/10.1006/icar.1998.6035

Sloughter, T., Banas, N., & Sambrotto, R. (2019). Seasonal variation in light response of polar phytoplankton. *Journal of Marine Systems*, *191*, 64–75. https://doi.org/10.1016/j.jmarsys.2018.12.003

Spitschan, M., Aguirre, G., Brainard, D., & Sweeney, A. (2016). Variation of outdoor illumination as a function of solar elevation and light pollution. *Scientific Reports*, *6*(1), 26756. https://doi.org/10.1038/srep26756

Stroeve, J., Vancoppenolle, M., Veyssiere, G., Lebrun, M., Castellani, G., Babin, M., et al. (2021). A multi-sensor and modeling approach for mapping light under sea ice during the ice-growth season. *Frontiers in Marine Science*, *7*, 1–28. https://doi.org/10.3389/fmars.2020.592337

Summers, N., Johnsen, G., Mogstad, A., Løvås, H., Fragoso, G., & Berge, J. (2022). Underwater hyperspectral imaging of Arctic macroalgal habitats during the polar night using a novel mini-ROV-UHI portable system. *Remote Sensing*, *14*(6), 1325. https://doi.org/10.3390/rs14061325

Veyssière, G., Castellani, G., Wilkinson, J., Karcher, M., Hayward, A., Stroeve, J. C., et al. (2022). Under-ice light field in the western Arctic Ocean during late summer. *Frontiers of Earth Science*, *9*, 1–19. https://doi.org/10.3389/feart.2021.643737

Wallace, M. I., Cottier, F. R., Berge, J., Tarling, G. A., Griffiths, C., & Brierley, A. S. (2010). Comparison of zooplankton vertical migration in an ice-free and a seasonally ice-covered Arctic fjord: An insight into the influence of sea ice cover on zooplankton behavior. *Limnology & Oceanography*, *55*(2), 831–845. https://doi.org/10.4319/lo.2009.55.2.0831